Journal of Materials Chemistry C

ROYAL SOCIETY OF CHEMISTRY

PAPER

View Article Online
View Journal | View Issue

Cite this: J. Mater. Chem. C, 2025, 13, 18981

Donor dilution in D18:L8-BO organic solar cells: visualization of morphology and effects on device characteristics

Bernadette C. Ortner, [ab] Konrad Binter,[b] Julia Hönigsberger,[b] Stefano Favero Costa,[c] Georg Haberfehlner, [a] Gerald Kothleitner, [ad] Heinz Amenitsch, [e] Thomas Rath, [b] Markus C. Scharber [c] and Gregor Trimmel *[b]

Received 10th June 2025,
Accepted 1st August 2025

DOI: 10.1039/d5tc02251g

rsc.li/materials-c

The increased interest in tandem solar cells and semitransparent building-integrated photovoltaics raises the need for organic solar cells with enhanced visible light transmittance. Reducing the donor content successfully enhances semitransparency in the visible wavelength range, however, it can introduce issues in charge carrier separation and transport. We address this key issue and concentrate on a detailed investigation of the nanomorphology of D18:L8-BO bulk heterojunctions with reduced donor content to provide new insights into the morphological changes and their impact on device performance. Scanning transmission electron microscopy combined with electron energy loss spectroscopy based elemental ratio mapping provides good contrast between the donor and acceptor domains and we observed that the donor phase forms a well interconnected network, which surprisingly persists even at low donor contents down to 2%. Investigations of the solar cell characteristics align with these findings and reveal that despite a significant reduction of the donor, the fundamental device physics remains largely unaffected. Rather than changes in charge carrier mobility or exciton dissociation, we identify charge carrier collection and a significant reduction in shunt resistance as critical loss factors that have been previously underestimated. A thorough understanding of these changes will contribute to optimizing donor-diluted organic solar cells for semitransparent applications.

1 Introduction

Organic solar cells are continually demonstrating enhancements and achieving unprecedented efficiencies. They are an intensively studied solar technology as they offer numerous advantages including cost-efficient manufacturing processes, excellent synthetic tunability of donor and acceptor properties, as well as the possibility for ultrathin, light-weight or semitransparent characteristics, stretchability and flexibility.[1–6] Accordingly, this solar cell technology is well suited for building-integrated photovoltaics (BIPV), agri-photovoltaics as well as for the use in tandem solar cells with semitransparency playing an important role.[3,7] For these applications, the absorption behavior must be tunable to either appear transparent for the human eye or offer suitable optical transmission for the second sub-cell in a tandem device. The characteristic absorption of active layer material combinations such as PM6:Y6 or D18:L8-BO is efficient over the entire visible spectrum up to the near infrared region, but can be influenced by changing donor to acceptor ratios (D : A ratios). With the donor absorbing in the visible range and the acceptor using mainly the NIR part of the solar spectrum, the average visible transmittance (AVT) can be improved with donor reduction.[3]

However, questions arise regarding the influence of donor dilution on the fundamental device physics, mode of operation, and power conversion efficiency. Unbalanced phase morphology, a reduced interface and, in the extreme case, the loss of percolation paths within the donor phase are consequences of this donor diluting approach. Exciton dissociation primarily occurs at the donor:acceptor (D:A) interface due to the energy level offset, therefore a reduced interfacial area results in less exciton dissociation and hampers the generation of free charge carriers.[8] The network formation typically witnessed for the

[a] Institute of Electron Microscopy and Nanoanalysis, NAWI Graz, Graz University of Technology, Steyrergasse 17, 8010, Graz, Austria
[b] Institute for Chemistry and Technology of Materials (ICTM), NAWI Graz, Graz University of Technology, Stremayrgasse 9, 8010, Graz, Austria. E-mail: gregor.trimmel@tugraz.at
[c] Linz Institute for Organic Solar Cells (LIOS), Institute of Physical Chemistry, Johannes Kepler University Linz, Altenbergerstrasse 69, 4040 Linz, Austria
[d] Graz Centre for Electron Microscopy, Steyrergasse 17, Graz, 8010, Austria
[e] Institute of Inorganic Chemistry, NAWI Graz, Graz University of Technology, Stremayrgasse 9, 8010 Graz, Austria

donor material D18 is beneficial for both, exciton dissociation and charge transport. Such networks are also found in other bulk heterojunction (BHJ) absorber layers (*e.g.* PM6:L8-BO, D18:L8-ThCl) and their investigation is mainly based on grazing-incidence wide-angle X-ray scattering (GIWAXS), atomic force microscopy (AFM) and transmission electron microscopy (TEM) in combination with electron diffraction techniques.[9–11] In previous work, it was shown that electron energy loss spectroscopy (EELS) enables efficient visualization of D:A separation in the bulk without crystallinity dependence, thereby enhancing the illustration of defined network structures.[12–15] These structures will be investigated more closely in this study focusing on changes resulting from gradual donor reduction in the D18:L8-BO system. D18:L8-BO is currently among the most efficient and thoroughly investigated material combinations that form network structures. To obtain a comprehensive understanding on the impact of the D : A ratios, this study investigates six weight ratios between 1 : 1.5 to 1 : 100. We correlate changes in the D:A network to photovoltaic parameters, absorption and EQE spectra, GIWAXS data, charge carrier mobility, J_{ph}–V_{eff} characteristics, light intensity dependence, and luminescence data. A particular focus is thereby set on elucidating how a systematic reduction of the donor fraction alters the underlying device physics.

2 Results and discussion

Solar cells with different D : A ratios were built in the configuration glass/ITO/PEDOT:PSS/active layer/PNDIT-F3N-Br/Ag with D18 as donor and L8-BO as acceptor material coated in form of a bulk heterojunction in various weight ratios. Following the idea of reducing the absorption in the visible light range, the concentration of D18 was reduced stepwise starting from 40 weight% (D : A 1 : 1.5, w : w), to 20% (1 : 4), 11% (1 : 8), 9% (1 : 10), 2% (1 : 50) and finally to 1% (1 : 100). Additionally, the pristine materials were tested regarding their photovoltaic performance in the same device architecture. The chemical structure of D18 and L8-BO, absorption spectra, *J*–*V* curves and the extracted photovoltaic parameters of the solar cells with different D : A ratios are depicted in Fig. 1 and the corresponding data are summarized in Table 1. Additionally, the absorption spectra (normalized) of the samples with different D : A ratios and the absorption spectra of the pristine materials are shown in Fig. S1.

According to Fig. 1c, the fill factor (FF) has a high tolerance to donor reduction across D : A weight ratios from 1 : 1.5 to 1 : 10 followed by a marked decline at ratios of 1 : 50 and 1 : 100. The open circuit voltage (V_{OC}) shows stable behavior over all investigated ratios, however, the ratio alteration provides notable impact on the short circuit current densities (J_{SC}). The J_{SC} values steadily decrease with reduced donor content, from 24.4 mA cm^{-2} (1 : 1.5) to 11.9 mA cm^{-2} (1 : 10) and 3.33 mA cm^{-2} (1 : 100). Despite a significant reduction of the donor content from 40% (1 : 1.5) to 9% (1 : 10), it is interesting to note that only a performance decline of about 50% is observed (15.8% to 7.5%). A similar correlation between solar cell performance and donor content was observed for the PM6:Y6 combination by Zhang *et al.*[16]

Significant variations depending on donor content alteration are observed in the absorption spectra shown in Fig. 1e. This graph demonstrates a substantial decline in the absorption of the visible range with decreasing donor content. The donor absorption peak maxima located between 570 and 600 nm are significantly decreasing with reduced donor content in comparison to the L8-BO absorption peak maxima located between 790 and 820 nm. For the 1 : 50 and 1 : 100 ratios, no significant changes are visible in the donor absorption region. However, depending on the processing conditions, absorption spectra of these two ratios can reveal a distinct

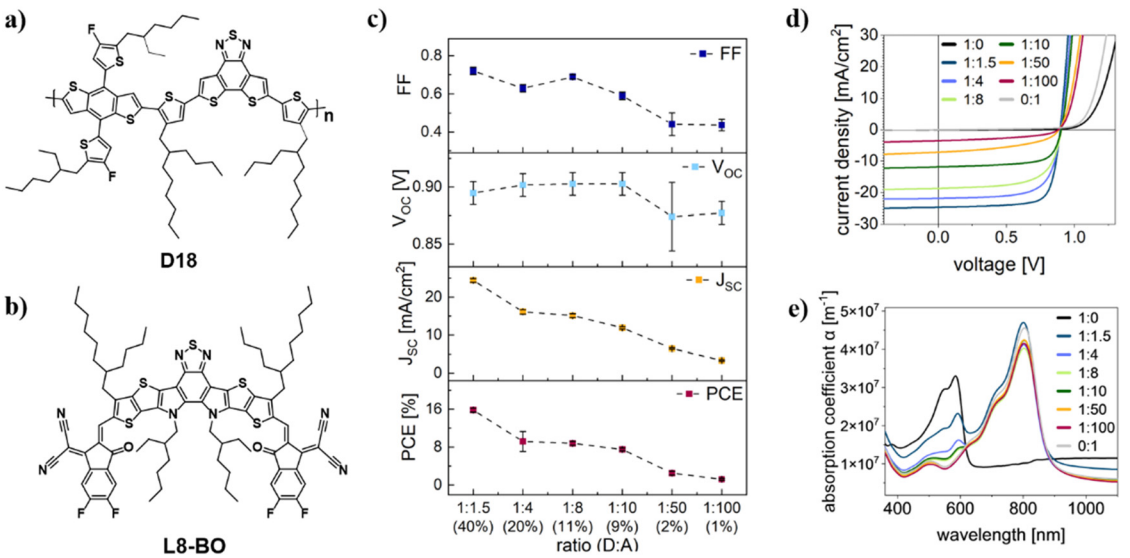

Fig. 1 Chemical structures of (a) D18, (b) L8-BO, (c) FF, V_{OC}, J_{SC} and PCE plotted *vs.* the D : A ratio, (d) *J*–*V* curves, measured under illumination, of solar cells with different D : A ratios and (e) their absorption spectra for the pure materials and the blends with different D18:L8-BO ratios from 1 : 1.5 to 1 : 100.

Table 1 Photovoltaic parameters determined from the *J–V* curves, J_{SC}/J_{sat} and J_{MPP}/J_{sat} extracted from J_{ph}–V_{eff} characteristics, and the mobility values determined from hole and electron-only devices *via* the SCLC method. The active layer thickness values were 87 nm (1 : 0), 88 nm (1 : 1.5), 99 nm (1 : 4), 102 nm (1 : 8), 107 nm (1 : 10), 115 nm (1 : 50), 100 nm (1 : 100) and 89 nm (0 : 1) varying in the range of ±5 nm for the different devices

Ratios	V_{OC} [V]	J_{SC} [mA cm^{-2}]	FF	PCE [%]	J_{SC}/J_{sat}	J_{MPP}/J_{sat}	μ_e [cm^2 V^{-1} s^{-1}]	μ_h [cm^2 V^{-1} s^{-1}]
1 : 1.5	0.90(0.89 ± 0.02)	24.8(24.4 ± 0.5)	0.73(0.72 ± 0.02)	16.4(15.8 ± 0.4)	0.97 ± 0.02	0.83 ± 0.07	$9.63 \times 10^{-4} \pm 2.14 \times 10^{-4}$	$4.98 \times 10^{-5} \pm 2.69 \times 10^{-5}$
1 : 4	0.91(0.90 ± 0.01)	17.2(16.1 ± 0.6)	0.72(0.63 ± 0.02)	11.3(9.2 ± 2.1)	0.96 ± 0.01	0.83 ± 0.01	$2.62 \times 10^{-3} \pm 3.32 \times 10^{-4}$	$1.45 \times 10^{-4} \pm 4.30 \times 10^{-5}$
1 : 8	0.91(0.90 ± 0.01)	15.9(15.1 ± 0.5)	0.69(0.69 ± 0.01)	10.0(8.8 ± 0.4)	0.89 ± 0.01	0.70 ± 0.03	$2.67 \times 10^{-3} \pm 4.78 \times 10^{-4}$	$6.43 \times 10^{-5} \pm 2.45 \times 10^{-5}$
1 : 10	0.90(0.90 ± 0.01)	12.2(11.9 ± 0.3)	0.69(0.59 ± 0.02)	7.6(7.5 ± 0.3)	0.89 ± 0.01	0.62 ± 0.09	$5.25 \times 10^{-4} \pm 4.65 \times 10^{-4}$	$5.66 \times 10^{-5} \pm 2.93 \times 10^{-5}$
1 : 50	0.88(0.87 ± 0.03)	6.77(6.44 ± 0.2)	0.46(0.44 ± 0.06)	2.7(2.5 ± 0.4)	0.54 ± 0.05	0.36 ± 0.03	$7.50 \times 10^{-4} \pm 4.41 \times 10^{-4}$	$9.09 \times 10^{-5} \pm 4.48 \times 10^{-5}$
1 : 100	0.88(0.87 ± 0.01)	3.49(3.33 ± 0.17)	0.45(0.43 ± 0.03)	1.4(1.2 ± 0.2)	0.43 ± 0.02	0.19 ± 0.01	$6.57 \times 10^{-4} \pm 1.35 \times 10^{-4}$	$7.03 \times 10^{-5} \pm 5.99 \times 10^{-5}$
1 : 0	0.66(0.70 ± 0.14)	0.12(0.08 ± 0.03)	0.31(0.30 ± 0.01)	0.02(0.02 ± 0.01)	—	—	$2.04 \times 10^{-6} \pm 3.15 \times 10^{-6}$	$7.12 \times 10^{-5} \pm 1.02 \times 10^{-4}$
0 : 1	0.09(0.04 ± 0.03)	0.04(0.03 ± 0.007)	0.27(0.25 ± 0.02)	$1.0 \times 10^{-3}(3.8 \times 10^{-4} \pm 3.7 \times 10^{-4})$	—	—	$1.22 \times 10^{-3} \pm 2.46 \times 10^{-4}$	$7.67 \times 10^{-5} \pm 2.87 \times 10^{-5}$

redshift of the acceptor absorption maxima from 800 nm to 817 nm as shown in Fig. S1a. This indicates a more pronounced crystallinity of the acceptor in these films compared to layers with a higher donor content and thereby possibly also a significantly changed D:A network formation.

For the *J–V* curves of the devices with 1 : 50 and 1 : 100 D : A ratios, in addition to a reduced photocurrent also the photovoltage and in particular the FF are significantly reduced, which demonstrates the competition between recombination and extraction of charge carriers.[17] Obviously, the series resistance (R_{series}) is also much higher for solar cells with these two ratios (1 : 50 and 1 : 100) and even more for those with the pure donor or acceptor. The R_{series} values are increasing from 1.7 Ω cm^2 (1 : 1.5) to 2.1 (1 : 4), 2.5 (1 : 8), 2.6 (1 : 10), 8.2 (1 : 50), 12.0 (1 : 100), 1990 (0 : 1) to 2960 Ω cm^2 (1 : 0). For more balanced D : A ratios (1 : 1.5, 1 : 4, 1 : 8 and 1 : 10), we believe that sufficiently efficient charge transport enables higher FFs and therefore decent efficiencies despite the significantly reduced donor content.

To better understand these results, we focused on the analysis of morphological changes induced by the variations in the D : A ratio, with particular attention on the investigation of the presence of percolation pathways for charge transport. Morphology investigations are typically done with techniques like TEM, AFM and PiFM (photo-induced force microscopy).[18,19] However, with STEM-EELS elemental mapping, which is used in this study, it is possible to distinguish between donor and acceptor materials based on their chemical composition.[20] Elemental ratio maps for nitrogen, present in higher amount in the acceptor (L8-BO ($C_{84}H_{90}F_4N_8O_2S_5$)), and for sulfur, present in higher amount in the donor material (D18 $(C_{76}H_{92}F_2N_2S_9)_n$), allow the visualization of the different phases, shown in Fig. 2. Since 7.77% N atoms are present in the acceptor molecule and 2.25% N atoms (H excluded) are present in the donor, there are 3.5 times more nitrogen atoms in the acceptor material. For the donor material, the sulfur content is 2.1 times higher than the one of the acceptor molecules with 4.85% sulfur in the acceptor *vs.* 10.11% sulfur in the donor. This enables the representation in elemental ratio maps, separating areas with different atomic ratios of a specific element, in this case nitrogen and sulfur. STEM-EELS data for D18 and L8-BO are shown in Fig. S2a. The mean relative thicknesses (t/λ) of the measured areas are 0.59 (1 : 1.5), 0.44 (1 : 4), 0.47 (1 : 8), 0.56 (1 : 10), 0.44 (1 : 50) and 0.54 (1 : 100) with λ representing the inelastic mean free path of electrons in the material and therefore (t/λ) representing the average number of inelastic scattering events per electron. Thickness estimation is done with a low-loss spectrum, comparing the intensity I_0 of the zero-loss peak with the total intensity I_t of the whole spectrum ($t/\lambda = \ln(I_t/I_0)$).[21] At constant experimental parameters, the mean free path λ depends mostly on the effective atomic number, which is similar for donor and acceptor, so it can be concluded that all samples have a similar thickness.

For the 1 : 1.5 ratio, a dense network structure with irregular sulfur- and nitrogen-rich areas are detected as shown in Fig. 2. The sulfur-rich donor material forms strand structures with a thickness of 15–20 nm. Regions used to estimate the diameter

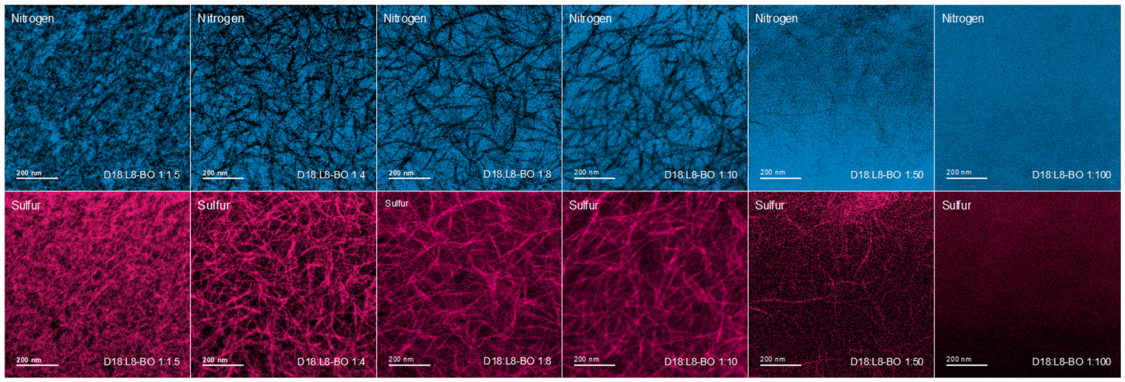

Fig. 2 Elemental ratio maps of N (blue) and S (red) based on STEM-EELS measurements of thin films with D : A ratios from 1 : 1.5 to 1 : 1 : 100 (w : w).

of the network strands are shown in Fig. S2b. Overall, an interpenetrating network on the nanoscale was clearly obtained, providing a large D:A interface for charge dissociation and a percolating structure for efficient charge transport.[22] The 1 : 4 sample shows a distinct sulfur content reduction, but nevertheless, a dense and regular network structure with polymer fibrils having a diameter between 15 and 27 nm. For the 1 : 8 and 1 : 10 ratios, the network density gets further reduced with 15–20 nm thick strands but also an increased appearance of 6–10 nm thin strands, especially for the 1 : 10 ratio. However, due to the elongated fibrils of D18, a percolating network can be assumed, enabling the relatively high FF obtained for solar cells with this ratio. Smaller photocurrents of the 1 : 10 compared to the 1 : 1.5 or 1 : 4 D : A ratio samples, can be explained with D : A interface reduction. For the 1 : 50 ratio, a very leaky network is still observed consisting of a few very thin donor threads, which measured approximately 10–15 nm. The presence of fibrils is heavily reduced, which hinders the charge transport in the donor phase due to the lack of percolating pathways. No donor network structure can be recognized in the 1 : 100 layer. Indeed, the solar cells based on these two D : A ratios show significantly higher series resistance and lower FF compared to the devices with higher donor content and prominent network structures.

In addition to the STEM-EELS analysis, AFM measurements were conducted and are depicted in Fig. S3 for all ratios. The films with D : A ratios of 1 : 1.5, 1 : 4 and 1 : 8 show fibrillar structures on the sample surface and for the 1 : 10 ratio, their visibility is significantly reduced, while for the films with 1 : 50 and 1 : 100 D : A ratios no similar network-like structures are detectable. The surface roughness values, shown in Table S1, significantly increase with the reduction of the donor material since the polymer does not flatten the film and larger acceptor domains are formed.

These results indicate that dense network structures of the donor are beneficial for obtaining a good fill factor with overall decreasing donor content, but do not prevent J_{SC} losses. Thus, the photocurrent generation was investigated in detail with external quantum efficiency (EQE) measurements. The EQE spectra in Fig. 3a also indicate the overall decreasing current generation and the peak maxima correlate with the maxima of the donor absorption peaks in the range of 500–600 nm. For the 1 : 1.5 ratio, the EQE spectrum in the donor absorbing region between 500 and 600 nm is slightly higher than in the acceptor absorbing area around 800 nm, which equalizes for higher ratios but never reverses to higher EQE values at around 800 nm despite increased L8-BO content. This might be caused by the formation of larger L8-BO aggregates between the donor

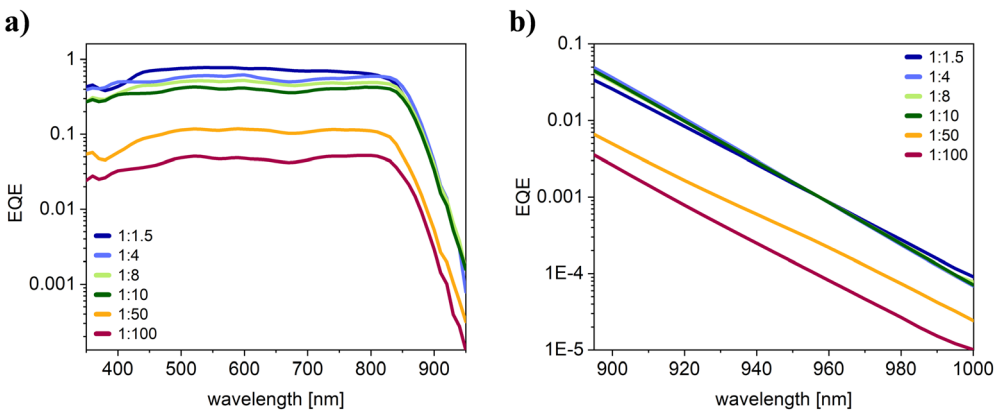

Fig. 3 (a) EQE spectra of solar cells with different D : A ratios in the active layer and (b) additional high sensitivity EQE measurements recorded between 895–1000 nm.

fibrils, which is also revealed by the EELS-based elemental ratio maps and known from literature.[19] The observation that the L8-BO in the larger aggregates is not efficiently contributing to the photocurrent generation could be caused by increased recombination within the large L8-BO domains exceeding the exciton diffusion length of approx. 14 nm (in pure L8-BO).[23,24] This is additionally supported by the enhanced photoluminescence (PL) of these devices (see below). The comparison of the calculated short circuit current densities from the EQE data with the measured J_{SC} values is given in Table S2.

The observations in the EQE spectra reveal that the donor material contributes significantly to photocurrent generation, even for absorber layers with lower donor content, but the donor reduction does not have a linear relationship with the J_{SC} values. Comparing the 1 : 1.5 (40% donor) and 1 : 100 (1% donor) D : A ratios, the donor content decreases by a factor of 40, while the short circuit current density is only reduced by a factor of 7.3 (1 : 1.5 ratio: 24.4 mA cm^{-2}; 1 : 10 ratio: 3.33 mA cm^{-2}). However, with regard to processability, the presence of a certain donor content is of considerable significance, because for pristine L8-BO, processing of homogeneous layers with reasonable thickness is very challenging. Therefore, the concentrations of the precursor solutions are increased from 4 mg ml^{-1} (1 : 0) to 8 (1 : 1.5), 14 (1 : 4), 16 (1 : 8 and 1 : 10) and 20 mg ml^{-1} (1 : 50, 1 : 100 and 0 : 1). The layer thicknesses were checked with a profilometer and the spin coating parameters adjusted accordingly to obtain layers of similar thickness.

Furthermore, the EQE spectra at the absorption edge between 895 and 1000 nm were analyzed in more detail to detect charge transfer states, but as it is shown in Fig. 3b, the curves for all ratios follow a linear decline with no visible appearance of the signature of charge transfer states. This is typical for D18:Y6 or other comparable absorber materials as the acceptor exciton and the charge transfer state show a very small energy offset.[25]

As already discussed above, the absorption spectra in Fig. S1a reveal a redshift for the acceptor peaks in the films with 1 : 50 and 1 : 100 D : A ratios. The redshift for ratios exceeding 1 : 10 could be caused by a closer packing and increased crystallinity of L8-BO resulting in pronounced inter-molecular electronic couplings as it is shown for Y6.[26] A denser π–π stacking typically results in enhanced charge transfer, charge separation and reduced energy losses.[27] But the significantly reduced D : A interface area in the samples with 1 : 50 and 1 : 100 D : A ratio, in combination with increased L8-BO domain sizes, might diminish these advantages. To investigate this in more detail, we characterized the films with grazing incidence wide-angle X-ray scattering (GIWAXS). The obtained GIWAXS images as well as the in-plane and out-of-plane cuts are shown in Fig. 4. It can be well observed that L8-BO has a lower π–π stacking distance compared to D18. The maximum of the π–π stacking peak of D18 is at 16.5 nm^{-1} (stacking distance: 0.38 nm), whereas the L8-BO reveals a maximum at 17.4 nm^{-1}, which corresponds to a π–π stacking distance of 0.36 nm. While the shape of the 1 : 10 sample is still similar to the samples with 1 : 4 and 1 : 8 ratios (with maxima of the π–π stacking peaks between 16.85 and 17.15 nm^{-1}), the 1 : 100 sample resembles the shape of the pristine L8-BO film very well and the maximum of the π–π stacking peak is very similar to the value of the pristine L8-BO film. Moreover, it can be observed that the L8:BO lamellar stacking distance in the blends remains unchanged compared to the pristine L8-BO film as indicated by the in-plane peak at 4.6 nm^{-1} corresponding to a lamellar stacking distance of 1.36 nm.

Furthermore, SCLC measurements of hole and electron only devices were performed (Fig. S4) and the obtained mobility values are summarized in Table 1 and Fig. 5a. We observed very comparable hole mobilities in the investigated D18:L8-BO blend films and even for pristine acceptor devices. This can be attributed to the ambipolar nature of L8-BO providing

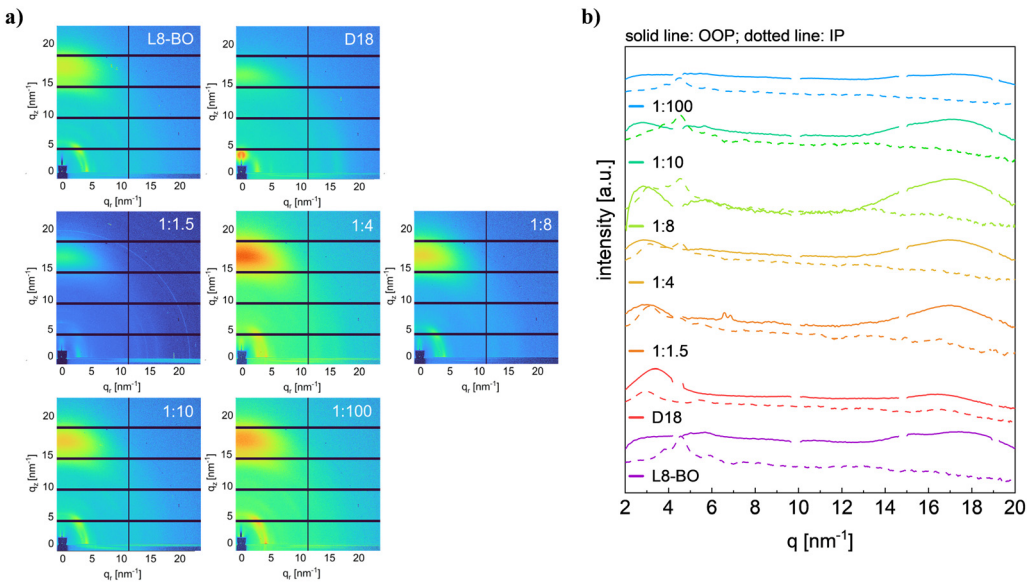

Fig. 4 (a) 2D-GIWAXS images of the pristine L8-BO and D18 films as well as the blends with different weight ratios (the blend with 1 : 50 ratio was not measured) and (b) the corresponding in-plane (IP) and out-of-plane (OOP) cuts.

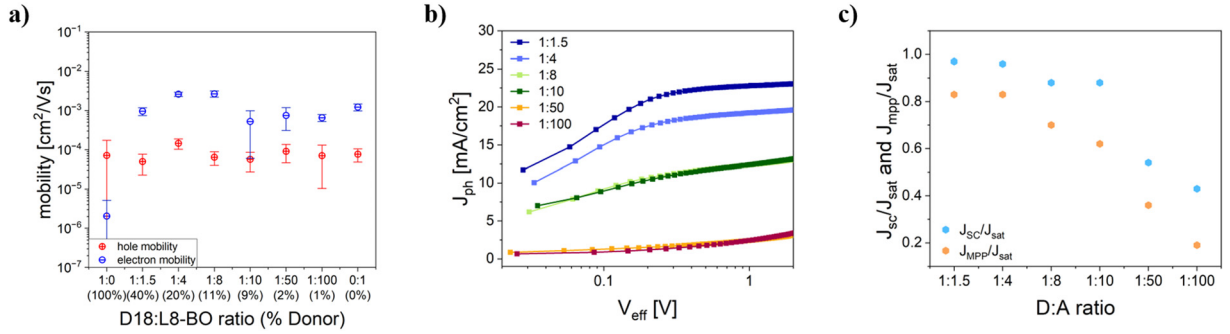

Fig. 5 Charge carrier mobilities for different D : A ratios (a), J_{ph}–V_{eff} characteristics (b) and the J_{SC}/J_{sat} and J_{MPP}/J_{sat} of the different ratios (c).

multiple charge-hopping channels and strong electronic coupling.[28] Also the electron mobilities have only a small correlation with varying the D : A ratios, except for pristine D18 devices, where a pronounced decrease in electron mobility is observed. For acceptor contents above 89% (1 : 8), the electron mobilities are decreasing. This trend was also found in PM6:Y6 cells with decreasing donor content.[16] It is assumed that the domain interconnectivity is reduced by increasing acceptor aggregation and thus has a significant negative effect on electron mobility[29] and is supported by the found increasing serial resistance. While these experiments reveal that the donor material is not a prerequisite for sufficient charge carrier mobilities, the loss of separate pathways for hole and electron transport enhances recombination in the active layers with low donor content.

Furthermore, J_{ph}–V_{eff} characteristics, as shown in Fig. 5b, were collected. The ratio of J_{SC} and J_{sat} (V_{eff} = 2 V) gives insight into the efficiency of exciton dissociation, while the ratio of the current density at the maximum power point (J_{MPP}) to J_{sat} provides information about the charge collection efficiency, both shown in Fig. 5c. The corresponding values are given in Table 1 and Table S3. Exciton dissociation stays above 0.88 for ratios up to 1 : 10, with a significant drop for the 1 : 50 and 1 : 100 ratios down to 0.54 and 0.43, respectively. In contrast, the charge collection efficiency in comparison to the exciton dissociation efficiency is decreasing more rapidly from 0.83 for 1 : 1.5 to 0.19 for 1 : 100. These results are in line with the reduction of the J_{SC} in these devices (*cf.* Table 1) and leads to the conclusion that approximately half of the losses in the 1 : 100 devices are caused by the fact that only half of the excitons (compared to the 1 : 1.5 device) dissociate and 80% of the generated charges are lost *via* nongeminate recombination due to insufficient charge transport.

Moreover, the recombination behavior was investigated with experiments on light intensity dependence of the J_{SC} shown in Fig. 6a and the V_{OC} (Fig. 6b). Alpha values derived from J_{SC} *vs.* light intensity measurements ($J_{SC} \propto I^{\alpha}$, with I for intensity) reveal information about recombination.[30] Interestingly, the alpha values derived from the linear fits, shown in Table S4, reveal values close to 1 for all the different ratios, validating balanced charge transport also shown in the SCLC measurements. However, V_{OC} measurements at different light intensities vary significantly for different D : A ratios. With decreasing light intensities, the V_{OC} of cells with ratios of 1 : 1.5 and 1 : 4 decreases quite linearly, while the voltage values for solar cells with lower donor content do not follow a linear trend. This could be caused by increased leakage currents with less donor content. The net current is comprised of the diode current, leakage current and the photogenerated current whereas all of them are voltage-dependent but only the latter scales with light intensity. As a consequence, the leakage current is of particular significance at lower light intensities.[31] The extent of leakage currents is predominantly influenced by the shunt resistances, which were determined from the dark curves for all different ratios. Shunt resistances decrease from 30.9 kΩ cm^2 (1 : 1.5) to 7.7 (1 : 4), 3.1 (1 : 8), 3.4 (1 : 10), 2.4 (1 : 50) and 2.1 kΩ cm^2

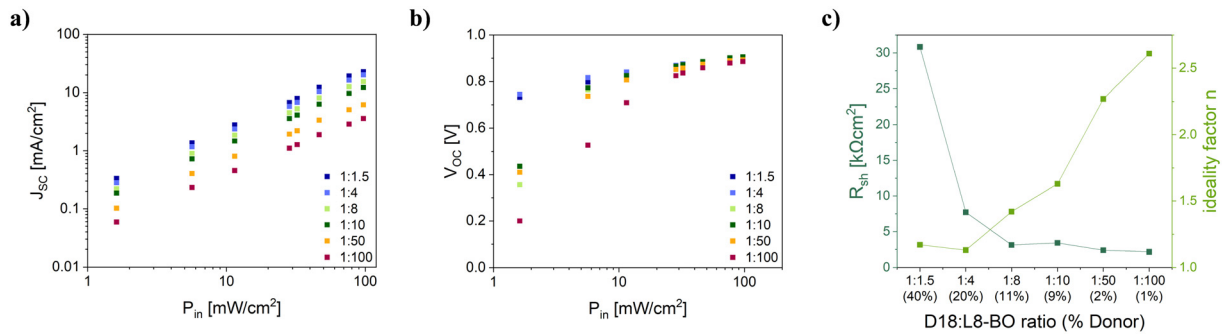

Fig. 6 Light intensity dependency of (a) J_{SC} and (b) V_{OC} of solar cells with different D18:L8-BO ratios and (c) shunt resistance (R_{sh}) and ideality factors n of the solar cells with different D : A ratios.

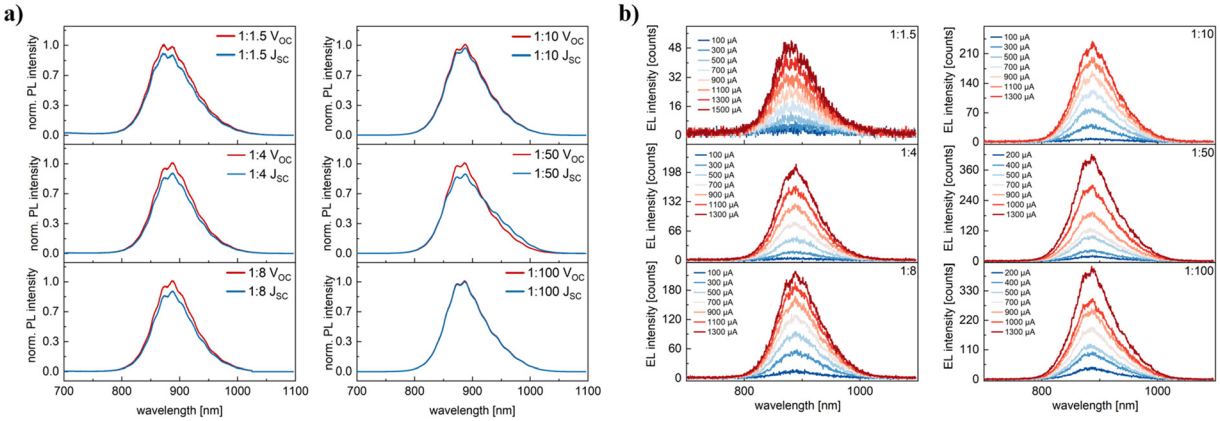

Fig. 7 Photoluminescence (PL) measurements of D18:L8-BO solar cells with different D : A ratios (a) and electroluminescence (EL) measurements with different applied currents (b).

(1 : 100), as shown in Fig. 6c, which could therefore confirm the problem with leakage currents. This makes it tricky to extract exact ideality factors, but an attempt was made to estimate the ideality factors from the data points at light intensities between approx. 100 and 30 mW cm^{-2}, as the V_{OC} dependence in this range shows a linear behavior and the results are shown in Fig. 6c and Table S4. For the 1 : 1.5 and 1 : 4 ratios, ideality factors close to 1 indicate that primarily bimolecular recombination occurs, while for the residual ratios, trap-assisted recombination gets increasing prominence, possibly caused by isolated donor island structures.[32]

The exciton recombination is further investigated with photoluminescence (PL) measurements. The different ratios are tested at open circuit and short circuit conditions plotted in Fig. 7a with the raw (not normalized) data in Fig. S5. The same energetic position of the photoluminescence peak in all samples suggests that the radiative recombination stems from the singlet exciton of the L8-BO. Minimal variation of the PL spectra recorded at V_{oc} and J_{sc} shows that only a fraction of charge carriers extracted under short circuit conditions recombine radiatively when the device is operated at open circuit. The observed emission origins from regions in the absorber layer where no charge generation is taking place and thus the photoluminescence increases with decreasing donor concentration (see Fig. S5), as larger L8-BO domains are formed. In these larger domains, photoexcitation predominantly leads to the formation of excitons, which recombine before they can be split at a D:A interface.

In addition to PL measurements, where laser excitation of charge carriers is used, electroluminescence (EL) measurements are performed with applied currents changing in the range from 100 to 1300 μA for the ratios 1 : 1.5, 1 : 4, 1 : 8 and 1 : 10 and 200 to 1300 μA for the ratios 1 : 50 and 1 : 100, shown in Fig. 7b. The electroluminescence matched the energetic position of the photoluminescence and increases exponentially in intensity with increasing injection currents.[25]

Reducing the donor concentration leads to higher EL intensities. In solar cells with a D : A ratio of 1 : 1.5, holes are predominately injected into the donor polymer and electrons are injected into the acceptor phase. Charge carriers recombine across the D:A interface mostly non-radiatively.

At low donor concentrations, electrons and holes are injected into the acceptor phase. As L8-BO supports the transport of electrons and holes, recombination of charges in the acceptor phase leads to the formation of L8-BO excitons. This is also supported by the bias-dependence of the electroluminescence (Fig. S6). While devices with D : A ratios between 1 : 1.5 and 1 : 10 show a steep increase of the EL between 0.8 and 0.9 V, much larger voltages are required to achieve similar EL intensities for lower donor concentrations.

3 Conclusion

To enable an in-depth investigation of donor diluted organic solar cells, D18:L8-BO bulk heterojunction solar cells were fabricated with six different donor to acceptor ratios. We focused thereby on the morphological changes in the active layer and its impact on device performance. Elemental ratio maps based on STEM-EELS measurements revealed the formation of donor networks down to donor contents of 2%, with decreasing extent but also alternating diameter of the donor fibrils with decreasing donor contents. These findings explain the less pronounced loss of power conversion efficiency with decreasing donor content compared to the significant reduction of visible light absorption in the donor absorption region between 400 and 600 nm. Charge carrier mobilities are nearly unaffected by donor content alteration thanks to the ambipolar nature of the L8-BO molecule. Down to a donor content to 9%, exciton dissociation efficiencies are stabilized by donor fibril thickness reduction preserving sufficient donor–acceptor interfacial area. The associated appearance of larger acceptor domains was reflected in the EQE spectra, as these domains are not contributing to photocurrent generation as expected. This assumption was supported by PL measurements, showing an increase in intensity with larger L8-BO domain sizes, but with minimal variation of the shape of the spectra recorded at V_{oc} and J_{sc}. Charge collection, on the other hand, showed higher sensitivity to donor content alterations

with trap-assisted recombination getting increased prominence with decreasing donor contents. Additionally, decreasing shunt resistances causing leakage currents were found to significantly impact the performance and therefore offering great potential for the improvement of solar cells with low donor content. This work serves as a foundation for understanding and addressing the challenges of donor-diluted organic solar cells, to enable targeted improvements and to optimize them for use in tandem solar cells or BIPV.

4 Experimental section/methods

4.1 Materials

The glass/ITO substrates were obtained from Luminescence Technology Corp., PEDOT:PSS (P VP AI 4083) was purchased from Heraeus Group and PNDIT-F3N-Br was purchased from 1-material. The conjugated polymers D18 as well as the NFA L8-BO were obtained from 1-material. Ag pellets were received from Kurt C. Lesker Company. The other materials and solvents used were obtained from VWR or Sigma-Aldrich/Merck.

4.2 Solar cell preparation

Glass substrates with a patterned ITO layer, the dimensions of 15 × 15 × 1.1 mm^3 and a sheet resistance of 15 Ω sq^{-1} were used. With tissues (Kimwipes, Kimberly-Clark) and acetone the cleaning of the substrates was done followed by sonication in a 2-propanol bath for 50 min at 40 °C. After blow-drying with nitrogen, oxygen plasma etching was done for 3 min at 99 W (FEMTO, Diener electronic). For solar cells built in the conventional architecture (ITO/PEDOT:PSS/donor:acceptor/PNDIT-F3N-Br/Ag), an aqueous PEDOT:PSS suspension was filtered through a syringe filter (0.45 μm PVDF). 50 μl of this solution were spin coated as the hole transport layer on the freshly plasma etched glass/ITO substrates with 3500 rpm (ramp: 1500 rpm) for 30 s. The films were thermally annealed in a glovebox under nitrogen atmosphere for 15 min at 150 °C. An average film thickness of 30 nm for the HTL was achieved. Solutions for the active layer were prepared by dissolving the donor and acceptor materials in chloroform (CF). The solutions were stirred overnight at room temperature and heated to 40 °C for 30 min in case of solubility problems, which was necessary, especially when working with D18. The active layers were applied with varying spin coating parameters (1000–5000 rpm; ramp: 2500 rpm), followed by thermal annealing under nitrogen atmosphere. The annealing temperature was 80 °C for 5 min. The electron transport layer was deposited on the absorber layer also in a glovebox under nitrogen atmosphere. Therefore, a PNDIT-F3N-Br layer was spin coated from a 0.5 mg ml^{-1} methanol solution with 2000 rpm (ramp: 1500 rpm) for 30 s. In the last step, the silver electrode was deposited *via* thermal evaporation also in a glovebox in a vacuum chamber. An electrode with 100 nm thickness was deposited with a deposition rate of 1 Å s^{-1} at a vacuum below 1 × 10^{-5} mbar (thickness monitor: Inficon SQM-160 rate/thickness monitor) through a 3 × 3 mm^2 shadow mask. Prior to EL, PL and EQE measurements, the solar cells were encapsulated to ensure stability under atmospheric conditions. For the encapsulation, the epoxy resin DELO® KATIOBOND® LP655 was applied onto 0.8 cm × 1.1 cm clean glass slides, which were then placed on the devices after approximately 50 seconds in an inert environment. The resin was cured for 4 min under 365 nm UV light.

4.3 TEM sample preparation and measurements

For investigations with the electron microscope the bulk heterojunction layer was spin coated on a sodium chloride crystal. The crystal was dissolved in deionized water and the floating films were washed several times and placed on a TEM Cu-grid. For the investigations with STEM-EELS, a probe-corrected FEI Titan^3 G2 60–300 equipped with a Gatan Imaging Filter (GIF) Quantum was used, operated at 300 kV. The beam current was ~100 pA and the collection semi-angle and convergence semi-angle were 25 and 19.6 mrad, respectively. The dispersion was set to 0.5 eV per ch to cover the L edge of sulfur at 165 eV and also the K edge of fluorine at 685 eV using the spectrometer in dual-EELS mode, with the core-loss spectrum covering the range of 120 to 1050 eV, roughly. Spectrum images have 300 × 300 pixels and were treated with simple denoise with PCA and component limiting. After PCA treatment, the ionization K-edges of the carbon (284 eV), nitrogen (402 eV), oxygen (532 eV), fluorine (685 eV) and the L-edge for sulfur (165 eV) are clearly visible. For the EELS edge setup, plural scattering was included correcting alterations in the edge shape and intensity caused by multiple scattering events with the low loss spectrum. For each pixel the signals are extracted and 2D elemental ratio maps are provided.

4.4 GIWAXS characterizations

These measurements were performed at the Austrian SAXS beamline 5.2L at the synchrotron ELETTRA (Trieste, Italy).[33] The setup uses a photon energy of 8 keV, a Dectris Pilatus3 1 M detector at a sample distance of 260 mm and an incident angle of 0.2°. The angular calibration was carried out using silver behenate powder (*d*-spacing of 58.38 Å) and p-bromo benzoic acid. The 1D line-cuts were calculated with the software SAXSDOG.[34] For the measurements, the compound films were prepared *via* spin coating on silicon substrates (grade: prime, thickness: 625 ± 20 μm, from Siegert Wafer) coated with a 25 nm PEDOT:PSS film. As background, the scattering pattern of a Si wafer with a PEDOT:PSS film was subtracted from the corresponding sample pattern.

Conflicts of interest

There are no conflicts to declare.

Data availability

The data supporting this article (additional details to experimental procedures and characterization techniques; information to data analysis; additional TEM/absorption data) have

been included as part of the SI. Supplementary information is available containing additional information to measurement procedures, absorption spectra, AFM measurements and additional PL data as well as EL-V and *J*–*V* plots. See DOI: **https://doi.org/10.1039/d5tc02251g**

Acknowledgements

Financial support by the Austrian Climate and Energy Fund and the Österreichische Forschungsförderungsgesellschaft mbH (FFG) within the program Energy Emission Austria (Project: PEROPTAM, FFG No. FO999896686) is gratefully acknowledged. Additionally, the authors thank the CERIC-ERIC Consortium for the access to experimental facilities of the Austrian SAXS beamline at Elettra Sincrotrone Trieste as well as financial support. The authors further thank Lukas Troi for the preparation of specific measurement setups as well as Virginia Lafranconi, Kevin Pree and Devina Gupta for their experimental support and Daniel Knez for helpful discussion.

References

1 S. Li, M. Gao, K. Zhou, X. Li, K. Xian, W. Zhao, Y. Chen, C. He and L. Ye, Achieving Record-High Stretchability and Mechanical Stability in Organic Photovoltaic Blends with a Dilute-absorber Strategy, *Adv. Mater.*, 2024, **36**, e2307278.

2 Y. Li, G. Xu, C. Cui and Y. Li, Flexible and Semitransparent Organic Solar Cells, *Adv. Energy Mater.*, 2018, **8**, 1701791.

3 F. Xue, Y. Xie, Y. Cui, D. Yu Paraschuk, W. Ma and H. Yan, Boosting Fill Factor of Semitransparent Donor-Poor Organic Solar Cells for the Best Light Utilization Efficiency, *Adv. Funct. Mater.*, 2024, **35**, 2415617.

4 B. Schweda, M. Reinfelds, P. Hofstadler, G. Trimmel and T. Rath, Recent Progress in the Design of Fused-Ring Non-Fullerene Acceptors-Relations between Molecular Structure and Optical, Electronic, and Photovoltaic Properties, *ACS Appl. Energy Mater.*, 2021, **4**, 11899–11981.

5 Z. Wang, X. Wang, L. Tu, H. Wang, M. Du, T. Dai, Q. Guo, Y. Shi and E. Zhou, Dithienoquinoxalineimide-Based Polymer Donor Enables All-Polymer Solar Cells Over 19% Efficiency, *Angew. Chem., Int. Ed.*, 2024, **63**, e202319755.

6 X. Li, A. Tang, H. Wang, Z. Wang, M. Du, Q. Guo, Q. Guo and E. Zhou, Benzotriazole-Based 3D Four-Arm Small Molecules Enable 19.1% Efficiency for PM6: Y6-Based Ternary Organic Solar Cells, *Angew. Chem., Int. Ed.*, 2023, **62**, e202306847.

7 Y. Li, X. Huang, H. K. M. Sheriff and S. R. Forrest, Semi-transparent organic photovoltaics for building-integrated photovoltaic applications, *Nat. Rev. Mater.*, 2023, **8**, 186–201.

8 P. Xue, J. Xin, G. Lu, B. Jia, H. Lu, G. Lu, W. Ma, R. P. S. Han and X. Zhan, High-performance semitransparent organic solar cells based on sequentially processed heterojunction, *J. Mater. Chem. C*, 2023, **11**, 8121–8128.

9 W. Köntges, P. Perkhun, J. Kammerer, R. Alkarsifi, U. Würfel, O. Margeat, C. Videlot-Ackermann, J.-J. Simon, R. R. Schröder, J. Ackermann and M. Pfannmöller, Visualizing morphological principles for efficient photocurrent generation in organic non-fullerene acceptor blends, *Energy Environ. Sci.*, 2020, **13**, 1259–1268.

10 K. L. Gu, Y. Zhou, W. A. Morrison, K. Park, S. Park and Z. Bao, Nanoscale Domain Imaging of All-Polymer Organic Solar Cells by Photo-Induced Force Microscopy, *ACS Nano*, 2018, **12**, 1473–1481.

11 H. Hu, Y. Li, J. Zhang, Z. Peng, L. Ma, J. Xin, J. Huang, T. Ma, K. Jiang, G. Zhang, W. Ma, H. Ade and H. Yan, Effect of Ring-Fusion on Miscibility and Domain Purity: Key Factors Determining the Performance of PDI-Based Nonfullerene Organic Solar Cells, *Adv. Energy Mater.*, 2018, **8**, 1800234.

12 S. Rechberger, N. Gasparini, R. Singh, M. Kim, C. L. Chochos, V. G. Gregoriou, K. Cho, C. J. Brabec, T. Ameri and E. Spiecker, Unraveling the Complex Nanomorphology of Ternary Organic Solar Cells with Multimodal Analytical Transmission Electron Microscopy, *Sol. RRL*, 2020, **4**, 2000114.

13 M. Pfannmöller, H. Flügge, G. Benner, I. Wacker, C. Sommer, M. Hanselmann, S. Schmale, H. Schmidt, F. A. Hamprecht, T. Rabe, W. Kowalsky and R. R. Schröder, Visualizing a homogeneous blend in bulk heterojunction polymer solar cells by analytical electron microscopy, *Nano Lett.*, 2011, **11**, 3099–3107.

14 S. F. Hoefler, G. Haberfehlner, T. Rath, A. Keilbach, M. A. Hobisch, A. Dixon, E. Pavlica, G. Bratina, G. Kothleitner, F. Hofer and G. Trimmel, Elucidation of Donor:Acceptor Phase Separation in Nonfullerene Organic Solar Cells and Its Implications on Device Performance and Charge Carrier Mobility, *ACS Appl. Energy Mater.*, 2019, **2**, 7535–7545.

15 P. Fürk, S. Mallick, T. Rath, M. Reinfelds, M. Wu, E. Spiecker, N. Simic, G. Haberfehlner, G. Kothleitner, B. Ressel, S. Holler, J. B. Schaubeder, P. Materna, H. Amenitsch and G. Trimmel, The challenge with high permittivity acceptors in organic solar cells: a case study with Y-series derivatives, *J. Mater. Chem. C*, 2023, **11**, 8393–8404.

16 N. Yao, J. Wang, Z. Chen, Q. Bian, Y. Xia, R. Zhang, J. Zhang, L. Qin, H. Zhu, Y. Zhang and F. Zhang, Efficient Charge Transport Enables High Efficiency in Dilute Donor Organic Solar Cells, *J. Phys. Chem. Lett.*, 2021, **12**, 5039–5044.

17 D. Bartesaghi, I. D. C. Pérez, J. Kniepert, S. Roland, M. Turbiez, D. Neher and L. J. A. Koster, Competition between recombination and extraction of free charges determines the fill factor of organic solar cells, *Nat. Commun.*, 2015, **6**, 7083.

18 L. Zhu, M. Zhang, J. Xu, C. Li, J. Yan, G. Zhou, W. Zhong, T. Hao, J. Song, X. Xue, Z. Zhou, R. Zeng, H. Zhu, C.-C. Chen, R. C. I. MacKenzie, Y. Zou, J. Nelson, Y. Zhang, Y. Sun and F. Liu, Single-junction organic solar cells with over 19% efficiency enabled by a refined double-fibril network morphology, *Nat. Mater.*, 2022, **21**, 656–663.

19 D. Li, N. Deng, Y. Fu, C. Guo, B. Zhou, L. Wang, J. Zhou, D. Liu, W. Li, K. Wang, Y. Sun and T. Wang, Fibrillization of Non-Fullerene Acceptors Enables 19% Efficiency Pseudo-Bulk Heterojunction Organic Solar Cells, *Adv. Mater.*, 2023, **35**, e2208211.

20 G. Haberfehlner, S. F. Hoefler, T. Rath, G. Trimmel, G. Kothleitner and F. Hofer, Benefits of direct electron detection and PCA for EELS investigation of organic photovoltaics materials, *Micron*, 2021, **140**, 102981.
21 R. F. Egerton, in *Electron energy-loss spectroscopy in the electron microscope*, ed. R. Egerton, Springer, New York, Heidelberg, 3rd edn, 2011, pp. 111–229.
22 K. Chong, X. Xu, H. Meng, J. Xue, L. Yu, W. Ma and Q. Peng, Realizing 19.05% Efficiency Polymer Solar Cells by Progressively Improving Charge Extraction and Suppressing Charge Recombination, *Adv. Mater.*, 2022, **34**, e2109516.
23 D. Qiu, M. A. Adil, K. Lu and Z. Wei, The Crystallinity Control of Polymer Donor Materials for High-Performance Organic Solar Cells, *Front. Chem.*, 2020, **8**, 603134.
24 F. Sun, X. Zheng, T. Hu, J. Wu, M. Wan, Y. Xiao, T. Cong, Y. Li, B. Xiao, J. Shan, E. Wang, X. Wang and R. Yang, 1,5-Diiodocyclooctane: a cyclane solvent additive that can extend the exciton diffusion length in thick film organic solar cells, *Energy Environ. Sci.*, 2024, **17**, 1916–1930.
25 J. Hofinger, C. Putz, F. Mayr, K. Gugujonovic, D. Wielend and M. C. Scharber, Understanding the low voltage losses in high-performance non-fullerene acceptor-based organic solar cells, *Mater. Adv.*, 2021, **2**, 4291–4302.
26 S. Mahadevan, T. Liu, S. M. Pratik, Y. Li, H. Y. Ho, S. Ouyang, X. Lu, H.-L. Yip, P. C. Y. Chow, J.-L. Brédas, V. Coropceanu, S. K. So and S.-W. Tsang, Assessing intra- and inter-molecular charge transfer excitations in non-fullerene acceptors using electroabsorption spectroscopy, *Nat. Commun.*, 2024, **15**, 2393.
27 X.-K. Chen, V. Coropceanu and J.-L. Brédas, Assessing the nature of the charge-transfer electronic states in organic solar cells, *Nat. Commun.*, 2018, **9**, 5295.
28 C. Li, J. Zhou, J. Song, J. Xu, H. Zhang, X. Zhang, J. Guo, L. Zhu, D. Wei, G. Han, J. Min, Y. Zhang, Z. Xie, Y. Yi, H. Yan, F. Gao, F. Liu and Y. Sun, Non-fullerene acceptors with branched side chains and improved molecular packing to exceed 18% efficiency in organic solar cells, *Nat. Energy*, 2021, **6**, 605–613.
29 Y. Li, D. Jiang, J. Sun, R. Shi, Y. Chen, M. Xu, X. Du, G. Xu and H. Yin, Acceptor aggregation induced hole mobility degradation in polymer solar cells, *J. Mater. Chem. A*, 2025, **13**, 19338–19344.
30 L. J. A. Koster, V. D. Mihailetchi, H. Xie and P. W. M. Blom, Origin of the light intensity dependence of the short-circuit current of polymer/fullerene solar cells, *Appl. Phys. Lett.*, 2005, **87**, 203502.
31 C. M. Proctor and T.-Q. Nguyen, Effect of leakage current and shunt resistance on the light intensity dependence of organic solar cells, *Appl. Phys. Lett.*, 2015, **106**, 083301.
32 S. Ryu, N. Y. Ha, Y. H. Ahn, J.-Y. Park and S. Lee, Light intensity dependence of organic solar cell operation and dominance switching between Shockley-Read-Hall and bimolecular recombination losses, *Sci. Rep.*, 2021, **11**, 16781.
33 H. Amenitsch, M. Rappolt, M. Kriechbaum, H. Mio, P. Laggner and S. Bernstorff, First performance assessment of the small-angle X-ray scattering beamline at ELETTRA, *J. Synchrotron Radiat.*, 1998, **5**, 506–508.
34 M. Burian, C. Meisenbichler, D. Naumenko and H. Amenitsch, SAXSDOG: open software for real-time azimuthal integration of 2D scattering images, *J. Appl. Crystallogr.*, 2022, **55**, 677–685.

